NANO LETTERS

pubs.acs.org/NanoLett Letter

High-Performance Two-Dimensional Perovskite $Ca_2Nb_3O_{10}$ UV Photodetectors

Yong Zhang, Siyuan Li, Ziliang Li, Hui Liu, Xinya Liu, Jiaxin Chen, and Xiaosheng Fang*

Cite This: *Nano Lett.* 2021, 21, 382–388 Read Online

ACCESS | Metrics & More | Article Recommendations | Supporting Information

ABSTRACT: We first report two-dimensional (2D) perovskite $Ca_2Nb_3O_{10}$ ultraviolet photodetectors (UV PDs), which are prepared via a facile calcination-exfoliation method. The 2D $Ca_2Nb_3O_{10}$ PDs demonstrate high performance at 3 V at 280 nm, high responsivity (14.94 A W^{-1}), high detectivity (8.7×10^{13} Jones), high spectral selectivity ($R_{280}/R_{400} = 8.84 \times 10^3$), fast speed (0.08/5.6 ms), and long-term stability, exceeding those of most reported UV PDs. Furthermore, the $Ca_2Nb_3O_{10}$ PDs integrated with poly(ethylene terephthalate) (PET) show excellent flexibility and have high linear dynamic range (96 dB). Our work provides a general strategy for searching new UV PDs based on numerous layered niobates. The $Ca_2Nb_3O_{10}$ nanosheets may be one of the optimum semiconductor materials for next-generation high-performance UV PDs.

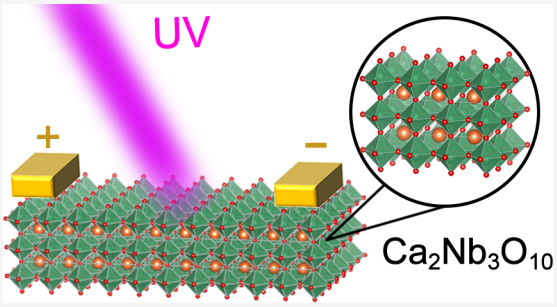

KEYWORDS: *$Ca_2Nb_3O_{10}$, UV photodetectors, two-dimensional, high performance*

Ultraviolet photodetectors (UV PDs) have always attracted extensive attention in many fields, such as space exploration, biological analysis, environmental sensors, communication, and imaging.[1−5] An ideal UV photodetector is generally expected to have high sensitivity, high detectivity, fast response speed, high spectral selectivity, high stability. For decades, numerous UV photodetectors based on traditional wide-bandgap semiconductors (ZnO, TiO_2, SnO_2, Ga_2O_3, GaN, etc.) have been extensively investigated.[6−10] Furthermore, extensive research efforts have been devoted to optimize the performance of these devices through a great variety of methods.[11−16] Recently, two-dimensional (2D) nanomaterials have drawn extensive attention because of their unique physicochemical properties and excellent photoelectric performances.[17−20] Meanwhile, halide perovskites have been proven to be outstanding candidates for optoelectronic devices.[21−24] These results give us suggestions to search for new 2D materials with perovskite structure for high-performance UV PDs. In addition, UV photodetectors with good flexibility can meet the future requirements of wearable electronics products. Therefore, it is essential to search for new materials for next-generation high-performance UV photodetection.

$KCa_2Nb_3O_{10}$ is an n-type semiconductor and has a layered perovskite structure, and it consists of negatively charged NbO_6 slabs and two adjacent slabs are separated by a layer of K^+ ion. Additionally, of particular interest are 2D $Ca_2Nb_3O_{10}$ (CNO) nanosheets, and a typical top-down approach based on high-temperature solid-state reaction followed by ion-exchange, intercalation, and exfoliation of layered products is the most commonly used method. These $Ca_2Nb_3O_{10}$ nanosheets have been proven as excellent materials for wide applications, such as dielectrics, ferroelectrics, photocatalysis, and water splitting.[25−30] In addition, $Ca_2Nb_3O_{10}$ nanosheets with wide band gap correspond with the UV photon energy range, and consequently, it could become a potential candidate for visible-blind photodetection. It has been reported that the Nb_2O_5 single nanoplate UV PD shows a high external quantum efficiency, and the $K_2Nb_8O_{21}$ single nanowire UV PD exhibits excellent sensitivity.[31,32] Up to now, there is no report on the photodetecting application of the $Ca_2Nb_3O_{10}$ nanosheets. Therefore, it is of significant importance to explore an efficient photodetection based on the $Ca_2Nb_3O_{10}$ nanosheets.

Herein, 2D $Ca_2Nb_3O_{10}$ nanosheets are prepared simply by solid-state reaction, ion-exchange, and exfoliation processes. The band gap of $Ca_2Nb_3O_{10}$ nanosheets is 3.85 eV, and the thickness of monolayer $Ca_2Nb_3O_{10}$ nanosheet is 1.8 nm. The $Ca_2Nb_3O_{10}$ nanosheets film photodetector exhibits high performance at 3 V at 280 nm light irradiation, including high responsivity, high detectivity, fast speed, excellent spectral selectivity, and high stability, which is superior to the most reported UV PDs. Furthermore, the $Ca_2Nb_3O_{10}$ nanosheets PD integrated with PET demonstrates excellent flexibility and outstanding performance. Our work provides a general strategy

Received: September 18, 2020
Revised: December 8, 2020
Published: December 18, 2020

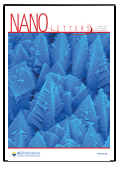

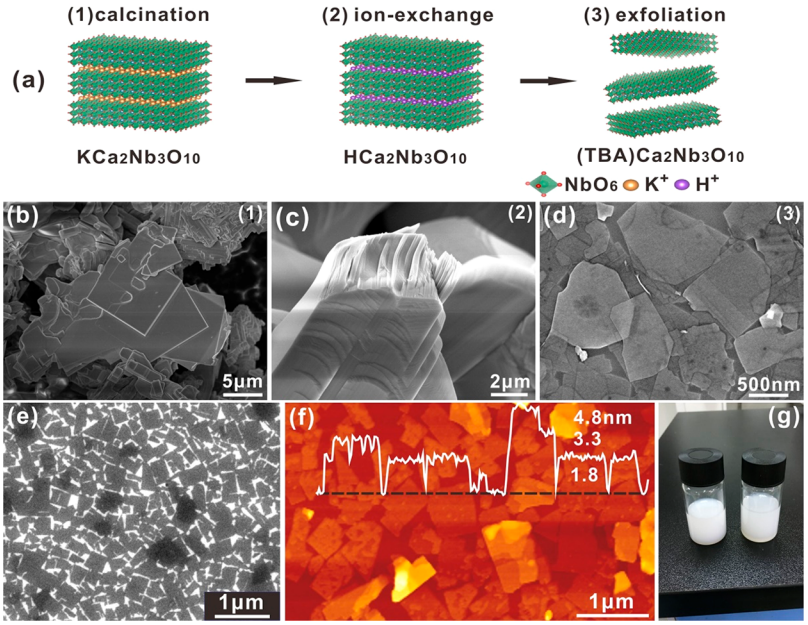

Figure 1. Morphology of $Ca_2Nb_3O_{10}$ nanosheets. (a) The diagrammatic sketch of the CNO nanosheets preparation process. (b–d) SEM images of KCNO sample after calcination (b), HCNO sample after ion-exchange (c), and CNO nanosheets after exfoliation (d). (e) SEM images of CNO nanosheets. (f) AFM image of CNO nanosheets and insert presents the height profile. (g) Photograph of $Ca_2Nb_3O_{10}$ nanosheets in deionized water.

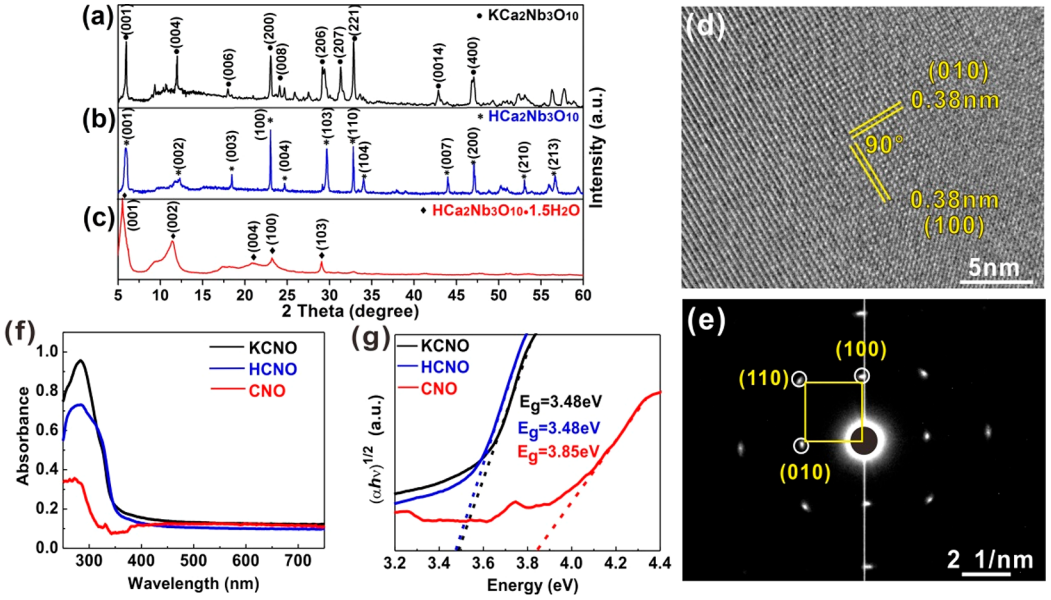

Figure 2. Structure and properties of CNO nanosheets. (a–c) XRD patterns of samples after calcination, ion-exchange, and exfoliation. (d,e) HRTEM image (d) and SAED pattern (e) of CNO nanosheets. (f,g) UV–vis absorption (f) and Tauc plot (g) of obtained KCNO, HCNO and CNO nanosheets.

for searching a new family of layer niobates as for high-performance UV PDs.

The $Ca_2Nb_3O_{10}$ nanosheets are prepared by simple solid-state sintering, ion-exchange, and exfoliation methods, as shown in Figure 1a. The scanning electron microscopy (SEM) images of each step of the products are displayed in Figure 1b–d. The first step is the preparation of $KCa_2Nb_3O_{10}$ (KCNO) samples via solid-state calcination. The KCNO crystals are well-crystallized, and the length of the large rectangular grains can reach up to 10 μm (Figure 1b). Subsequently, the $HCa_2Nb_3O_{10}$ (HCNO) samples are obtained by replacing K^+ of KCNO samples with H^+ in nitric acid, with a well-defined layered structure (Figure 1c). After an exfoliated process, the ultrathin 2D CNO nanosheets are obtained, as presented in Figure 1d. The length of CNO nanosheets ranges from 500 to 1000 nm (Figure 1e), and the thickness of monolayer CNO nanosheet with three layers NbO_6 octahedra is measured to be 1.8 nm according to the atomic force microscope (AFM) image (Figure 1f).[26] Therefore, 2D monolayer or few-layer CNO nanosheets are successfully prepared, and they present good dispersion and stability in water (Figure 1g). The simple and atoxic, low-cost,

https://dx.doi.org/10.1021/acs.nanolett.0c03759
Nano Lett. 2021, 21, 382–388

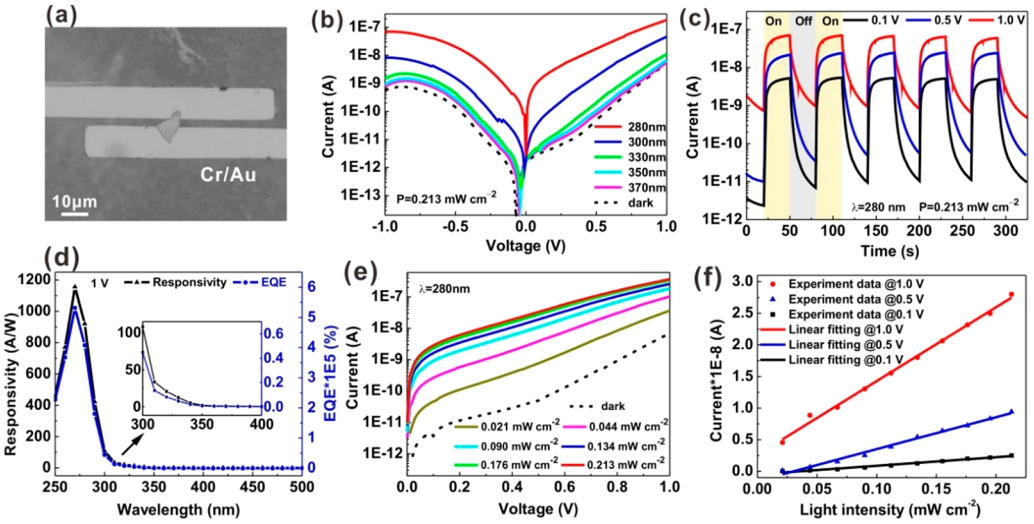

Figure 3. Photodetecting performance of the CNO single nanosheet PD. (a) The optical photograph of the device. (b) $I-V$ curves of the device under different wavelengths. (c) $I-t$ curves for the device at different bias voltages. (d) The responsivity and EQE for the device. (e) $I-V$ curves for the device with different incident light densities. (f) The variation of photocurrent and the linear fitting curves for the device.

and large-scale preparation of 2D CNO nanosheets makes it advantageous for fabricating various optoelectronic devices.

The X-ray diffraction (XRD) technique is utilized to reveal the phase structure of products after solid-state calcination and ion-exchange. Note that grazing incidence X-ray diffraction (GIXRD) pattern is carried out for the exfoliated CNO nanosheets. As displayed in Figure 2a–c, the crystal phases of specimens change substantially during the preparation process. For the sample after calcination, the strong peaks at 5.8°, 12.0°, 23.1°, 29.4°, 31.3°, and 32.9° match well with the (001), (004), (200), (206), (207), and (221) planes of $KCa_2Nb_3O_{10}$ (JCPDS 35-1294) (Figure 2a). In ion-exchange process, the $HCa_2Nb_3O_{10}$ is formed. Additionally, the four strongest peaks appear in Figure 2b centered at 6.1°, 23.1°, 29.7° and 32.9° corresponding to (001), (100), (103), and (110) planes of tetragonal $HCa_2Nb_3O_{10}$ (JCPDS 40-0884). Furthermore, the GIXRD pattern of the exfoliated CNO nanosheets displays strong diffraction peaks at 5.4° 10.9°, 23.1°, and 28.4°, corresponding to (001), (002), (100), and (103) planes of $HCa_2Nb_3O_{10}\cdot 1.5H_2O$ (JCPDS 39-0915), as shown in Figure 2c. In addition, the existence of the elements (Ca, Nb, and O) on the exfoliated CNO nanosheets surface is confirmed by X-ray photoelectron spectroscopy (XPS) pattern, as illustrated in Figure S1 (Supporting Information). The phase structure of the obtained CNO nanosheets is further characterized by high-resolution transmission electron microscope (HRTEM) pattern. The sharp edges of a rectangular sheet could be clearly observed in Figure S2 (Supporting Information). The interplanar spacing along two perpendicular directions are both measured to be 0.38 nm, corresponding to the (100) and (010) planes of the CNO nanosheet (Figure 2d). Furthermore, the selected area electron diffraction (SAED) measurement presented in Figure 2e could be indexed to be (100), (010) and (110) planes, in agreement with the lattice plane data measured by HRTEM. As shown in Figure 2f, compared with KCNO and HCNO, the absorption edge of the CNO nanosheets shows remarkable blue shift with the decreased thickness, attributing to the quantum size effect. From the corresponding UV–vis absorbance spectroscopy, the band gaps of KCNO, HCNO, and CNO sheets are calculated to be 3.48, 3.48, and 3.85 eV separately, as shown in Figure 2g. In addition, the valence band edge of CNO locates at 2.57 eV (see Figure S3; Supporting Information), which is lower compared with the Fermi energy band. The sample gives Raman bands at around 578, 765, and 948 cm^{-1}, corresponding to the Raman bands signal intensities of the Nb–O, Nb–OH, and Nb=O, respectively[33] (Figure S4, Supporting Information). Moreover, the weightlessness process of CNO nanosheets can be divided into three stages, attributing to the loss of surface water, the loss of interlayer water, and the decomposition of tetrabutyl ammonium $(TBA)^+$ (Figure S5, Supporting Information).

The photodetecting performances of $Ca_2Nb_3O_{10}$ nanosheets are characterized by fabricating a $Ca_2Nb_3O_{10}$ single nanosheet photodetector via a typical photolithography, deposition of Cr/Au electrodes and lift-off process, and the optical photograph of the photodetector is presented in Figure 3a. The average thickness of the CNO nanosheet is 80 nm from the AFM image (Figure S6, Supporting Information). Figure 3b exhibits the current–voltage ($I-V$) features of CNO single nanosheet photodetector in a logarithmic plot in dark and under light irradiation with various wavelengths. The device exhibits a dark current (5.52 nA) and yields a markedly enhanced photocurrent (182.9 nA) at 1 V at 280 nm. Figure 3c exhibits the photocurrent response characteristics of the CNO single nanosheet PD under 280 nm light at various bias voltages. The current–time ($I-t$) curves of the device show outstanding reproducibility and stability. As the UV light is turned on and off, the photocurrents increase to 5, 25, 64 nA and decreases to 10, 56, 732 pA at 0.1, 0.5, 1.0 V bias, respectively. In order to evaluate the photoelectric performance of the CNO single nanosheet PD, two important parameters (i.e., the spectral responsivity (R_λ) and external quantum efficiency (EQE)) have been calculated following the equations:

$$R_\lambda = \frac{I_{ph} - I_d}{P_\lambda S} \tag{1}$$

$$\mathrm{EQE} = R_\lambda \frac{hc}{e\lambda} \tag{2}$$

https://dx.doi.org/10.1021/acs.nanolett.0c03759
Nano Lett. 2021, 21, 382–388

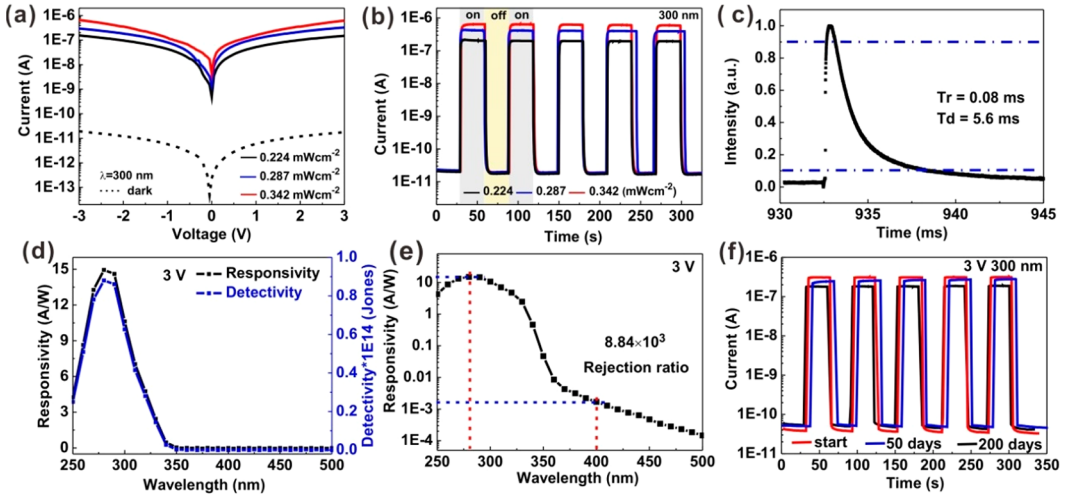

Figure 4. Photodetecting performance of the CNO nanosheets film PD. (a) $I-V$ curves for the device with different incident power densities. (b) $I-t$ curves for the device under 300 nm light switching. (c) The normalized pulse response of the device. (d) The responsivity and detectivity for the device. (e) The responsivity of the device in a log coordinate. (f) $I-t$ curves for the device after various days.

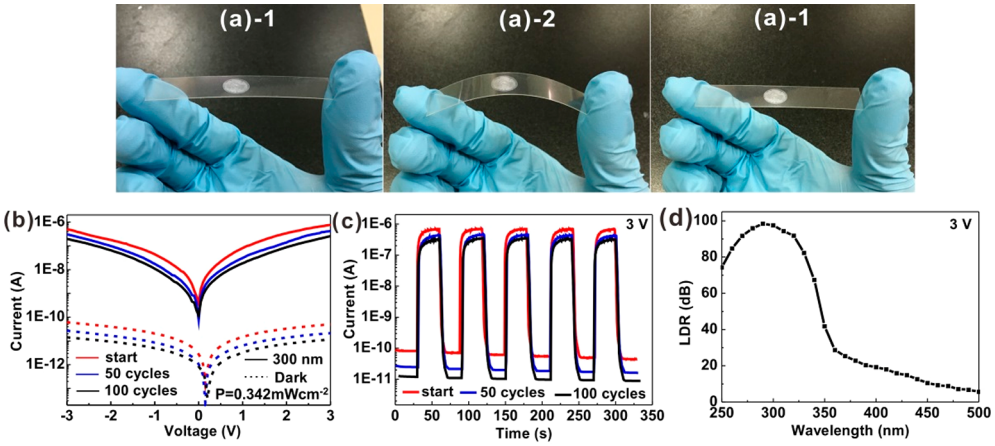

Figure 5. Photodetecting performance of the flexible CNO nanosheets film PD under 300 nm light irradiation. (a) The photograph of flexible CNO@PET PD with a single bending cycle. (b,c) $I-V$ curves (b) and $I-t$ curves (c) of the PD after various bending cycles. (d) The linear dynamic range spectrum of the PD.

where I_{ph} and I_d represent the photo and dark current, respectively, P_λ is the light power density of the incident light with the wavelength of λ, S is the effective area, and h represents the Planck's constant, c and e represent the velocity of light and electronic charge, respectively. Figure 3d shows that the responsivity of CNO single nanosheet photodetector can reach up to 1156 A W^{-1} at 270 nm at 1 V thanks to the high level of photocurrent and rather small exposure area between two metal contacts, which is much higher than that of niobate UV PDs, such as Nb_2O_5 single nanoplate (24.7 A W^{-1}) and $K_2Nb_8O_{21}$ single-nanowire PDs (2.53 A W^{-1}).[31,32] Meanwhile, the EQE of the device is measured as high as 5.32 × 10^5% at 270 nm at 1 V (Figure 3d). Figure 3e displays the $I-V$ features of the CNO single nanosheet PD at 280 nm with different power densities. When the power density of the light illumination is set as 0.021 to 0.044, 0.090, 0.134, 0.176, and 0.213 mW cm^{-2}, a corresponding photocurrent of 36.5, 101.8, 183.7, 257.3, 329.0, and 366.3 nA can be obtained. The relationship of the photocurrent with light intensity can be fitted by a power law, that is, $I_{ph} = AP^\theta$, where A is a constant and the exponent θ determines the response of the photocurrent to irradiation intensity. As shown in Figure 3f, the linear fit is quite satisfactory to describe the correlation at 0.1, 0.5, and 1.0 V. These results demonstrate that the CNO single nanosheet photodetector is an excellent visible-blind PD.

Further investigation is carried out to examine the performance of CNO nanosheets film by fabricating photodetector via drop coating on quartz substrate and deposition of Cr/Au electrodes by mask, as schematically illustrated in Figure S7 (Supporting Information). Figure 4a exhibits the $I-V$ features of CNO nanosheets film photodetector with variable power densities. It is noteworthy that the PD presents a low dark current (17.8 pA), and the photocurrents reach up to 0.63 μA at 300 nm. Specifically, compared with the dark current at 3 V, the photocurrent of the device is greatly enhanced. Figure 4b exhibits the $I-t$ characteristics of CNO nanosheets film photodetector with variable power densities at 300 nm at 3 V, and the device shows fast photoresponse and good reproducibility. As the UV light switched (0.342 mW cm^{-2}), the photocurrent of the photodetector quickly increases to 0.62 μA and then quickly decreases to 18.4 pA. The on/off ratio (I_{ph}/I_d) of this device is calculated to be as high as 3.4 × 10^4 at 3 V. Figure 4c displays a normalized time-resolved response curve of a single period of the pulse response, where

https://dx.doi.org/10.1021/acs.nanolett.0c03759
Nano Lett. 2021, 21, 382−388

the rise and decay time can be estimated to be ~0.08 and ~5.6 ms, respectively. Furthermore, the detectivity (D^*) can be estimated by the following equation:

$$D^* = \frac{R_\lambda}{(2eI_d/S)^{1/2}} \quad (3)$$

The responsivity and detectivity of CNO nanosheets film photodetector are presented in Figure 4d at 3 V with the wavelength from 500 to 250 nm. The maximum responsivity of the device is up to 14.94 A W^{-1} at 280 nm. The photodetector displays an ultrahigh detectivity because of the low dark current and high photocurrent, and the calculation value reaches up to 8.7×10^{13} Jones at 3 V at 280 nm (Figure 4d). The UV/visible rejection ratio (R_{280}/R_{400}) of this visible-blind photodetector is measured to be 8.84×10^3 (Figure 4e), which indicates ultrahigh spectral selectivity in the visible-blind region. As shown in Figure 4f, the CNO nanosheets film PD demonstrates long-term stability over 200 days in the surrounding environment. These results indicate that the CNO nanosheets film device has the optimized performances as a visible-blind photodetector.

The potential of CNO nanosheets for constructing flexible photodetectors is explored by dropping CNO nanosheets on PET (CNO@PET). Further investigation is conducted to examine the photodetecting performance of CNO@PET flexible device. The photograph of flexible CNO@ PET device is presented in Figure S8 (Supporting Information). When 300 nm light illuminated after a certain bending angle, the photocurrents of the CNO@PET photodetector are measured for various circles, as shown in Figure 5a. Figure 5b exhibits the $I-V$ features of CNO@PET PD with variable bending circles. Note that both photocurrent and dark current degrade slightly during the bending process of the device. Figure 5c exhibits the $I-t$ features of the CNO@PET photodetector irradiated after different bending circles, and the device shows high stability and repeatability. As seen in Figure 4a,b and Figure 5b,c, the CNO device fabricated on PET shows negligible photocurrent decline compared with the CNO device fabricated on quartz and also has a relatively slow response speed. After many bending circles, the stacking and cross-linking CNO nanosheets will slide and deform, which may hinder the transport of photogenerated carriers between adjacent nanosheets. Therefore, the resistance of the flexible CNO device increases and the dark current of the CNO flexible device decreases with increasing the bending cycles, as shown in Figure 5c. This is also sharing the main responsibility for the flexible CNO device with relatively slow speed. Additionally, the linear dynamic range [LDR(dB) = $20\log(I_{ph}/I_d)$] is also an important merit for a PD, and the result is shown in Figure 5d. The LDR is measured up to 96 dB under 280 nm light irradiation, which is much higher than that of ZnO UV photodetector (73 dB).[34] In addition, the work mechanism of the PD can be interpreted by a simple energy band diagram, as shown in Figure S9. In dark, the electron transport in the channel is mainly decided by contact barriers, making the PD in an equilibrium state. While under UV light illumination, the photocurrent increases linearly and the CNO Fermi level downshifts, leading to a higher energy barrier at two small contact interfaces. In this scenario, the photocurrent can dominate in the channel, which reveals a high sensitivity to UV light irradiation. Moreover, the electronic structure of an $HCa_2Nb_3O_{10}$ monolayer was carried out by the density functional theory (DFT) calculations (Figure S10 and Figure S11 for optimized structures and charge density distribution, respectively, Supporting Information). Although the DFT calculations usually underestimate the band gap (3.66 eV, as shown in Figure S12a), they can provide valid information related to the contribution of atomic orbitals and the trend of energies. The results from the density of states analysis (Figure S12b) discloses that the 3d orbitals of the Nb and the 2p orbitals of the O contribute mostly to the conduction band and valence band, respectively.[35]

The CNO nanosheets film UV PDs show optimized photoelectric performances, exceeding most of the previously reported UV PDs (Tables S1 and S2, Supporting Information). Table S1 displays a list of comparison of the main parameters for CNO film UV PD and other pure material UV PDs in literature. Table S2 provides a summary and comparison of the main parameters for CNO film PD and other composite materials UV PDs. For cost-effective and environmental friendliness, the CNO nanosheets can be large-scale prepared via a simple calcination-exfoliation process, which rules out high-end expensive equipment (Molecular Beam Epitaxy), tedious complicated process (Magnetron Sputtering), precise parameter control (Chemical Vapor Deposition). For sensitivity, the CNO film PD has much higher responsivity than that of SiC and MgZnO PDs. The high photocurrent of 620 nA is much larger than that of ZnS and Nb_2O_5 devices. For detectivity, this device exhibits an ultrahigh detectivity of 8.7×10^{13} Jones, exceeding the latest reported 2D $Ga_2In_4S_9$ flake and CuBr flake devices. For spectral selectivity, the CNO film PD shows a larger UV/visible rejection ratio ($R_{280}/R_{400} = 8.84 \times 10^3$) than that of ZnO-$Ga_2O_3$ device ($R_{254}/R_{400} = 1.2 \times 10^3$).[36] For speed, compared with ZnO or SnO_2 PDs which usually exhibit slow response time (~10 s) because of the influence of surface oxygen molecules adsorption and desorption, this device has a much faster response speed of 0.08/5.6 ms. For stability, the CNO film device has long-term stability, which is superior to some 2D materials (black phosphorus, InSe nanosheets)[37,38] and hybrid perovskites.[39,40] For flexibility, the CNO film devices integrated with various flexible substrates (PET, filter paper, cotton thread) can be facilely fabricated to meet the future requirements of wearable electronics and intelligent equipment. For function expansion, the CNO nanosheets dispersed in water can be interacted with other materials to achieve special properties and unique function via facile immersion, drop coating, spraying, and self-assembly methods. Additionally, for specific physicochemical properties, unlike general 2D materials with van der Waals force, the CNO nanosheets both have the characteristics of 2D materials and perovskite materials with many intriguing and unique properties, such as ion shielding effect. Therefore, the $Ca_2Nb_3O_{10}$ nanosheets may be one of the most potential semiconductor materials for next-generation high-performance UV PDs.

In summary, 2D perovskite $Ca_2Nb_3O_{10}$ nanosheets are prepared via a facile calcination-exfoliation process. The $Ca_2Nb_3O_{10}$ nanosheets film PD shows high performance at 3 V at 280 nm, high responsivity (14.94 A W^{-1}), high detectivity (8.7×10^{13} Jones), high spectral selectivity ($R_{280\ nm}/R_{400\ nm} = 8.84 \times 10^3$), fast speed (0.08/5.6 ms), and long-term stability, enabling it meeting the basic requirements of an ideal UV PD. The 2D $Ca_2Nb_3O_{10}$ may be one of the optimized material candidates for next-generation high performance UV PDs, and

https://dx.doi.org/10.1021/acs.nanolett.0c03759
Nano Lett. 2021, 21, 382−388

paves an effective way for its wide applications in the optoelectronic technology and information industry.

EXPERIMENTAL SECTION

Synthesis of $Ca_2Nb_3O_{10}$ Nanosheets. The $Ca_2Nb_3O_{10}$ nanosheets were prepared by a typical calcination-exfoliation process. The mixture of K_2CO_3 (99.99%), $CaCO_3$ (99.99%), Nb_2O_5 (99.99%) with molar ratio of K:Ca:Nb = 1.05:2:3 was calcinated at 1223 K for 1 h in atmosphere after fully ground for 0.5 h. After that the product was fully ground for another 0.5 h, and $KCa_2Nb_3O_{10}$ was synthesized by calcinating the product at 1423 K for 10 h in atmosphere. The loss of alkali metal carbonate at high temperature was compensated by an excess amount of K_2CO_3. The ion-exchange process which replaces K^+ with H^+ was performed by stirring 0.5 g of $KCa_2Nb_3O_{10}$ powder and 20 mL of 5 M HNO_3 for 4 days, and the acid should be renewed every day. The $HCa_2Nb_3O_{10}$ sample was washed many times with deionized water before dispersion in aqueous solution with an equimolar amount of TBAOH hydroxide (25% aqueous solution, tetrabutylammonium). Then the $Ca_2Nb_3O_{10}$ nanosheets were exfoliated by slowly shaking the TBAOH solution at 120 rpm for 1 week in atmosphere. The unexfoliated $Ca_2Nb_3O_{10}$ sediment was removed by settling the suspension, and the $Ca_2Nb_3O_{10}$ nanosheets were washed three times and collected by centrifugation. The whole experimental process is simple and controllable, so the preparation of the $Ca_2Nb_3O_{10}$ nanosheets has good repeatability.

Characterization of $Ca_2Nb_3O_{10}$ Sample. The morphology and size of CNO nanosheets was confirmed by scanning electron microscopy (SEM, Zeiss Sigma). The height of the CNO nanosheets was carried out by atomic force microscopy (AFM, Bruker Multimode Catalyst). The phase structure of the products was recorded by X-ray diffraction (XRD, Bruker D8-A25) and grazing incidence X-ray diffraction (GIXRD, Rigaku Smartlab). The structure of CNO nanosheets was performed by high-resolution transmission electron microscopy (HRTEM, JEM-1400plus). The elemental composition of the CNO nanosheets was characterized by X-ray photoelectron spectroscopy (XPS, PHI 5000C ESCA). The light absorption property was investigated by UV−vis spectrophotometer (Hitachi, U-3900H).

Calculation Method. The VASP program and PBE functional was employed for all density functional theory (DFT) calculations. The monolayer $HCa_2Nb_3O_{10}$ model was created from the experimental crystal structure (ICSD collection code: 244333). Geometries were fully optimized with ENCUT of 500 eV and a 4*4*1 Gamma k-point mesh. The band structure was obtained using the hybrid functional HSE06 based on the optimized structure. The convergence energy threshold of 10^{-5} eV is applied in the self-consistent calculation. When the maximum stress of each atom is within 0.02 eV/Å, the equilibrium lattice constants are optimized.

Photoelectric Measurements. The $Ca_2Nb_3O_{10}$ single nanosheet photodetector was constructed by photolithography, electron beam deposition and lift-off. The photolithography was carried out by the Heidelberg μPG 501 direct writer system, and the photoelectric performance was conducted by the program controlled semiconductor characterization system (Keithley 4200, USA). Additionally, the pulse response was recorded by the digital oscilloscope (Tektronix DPO 5140B) equipped with a 355 nm Nd:YAG pulsed laser source.

ASSOCIATED CONTENT

Supporting Information

The Supporting Information is available free of charge at https://pubs.acs.org/doi/10.1021/acs.nanolett.0c03759.

Additional structure, morphology, and properties of $Ca_2Nb_3O_{10}$ nanosheets, along with material calculations and the comparison data (Table S1 and Table S2) (PDF)

AUTHOR INFORMATION

Corresponding Author

Xiaosheng Fang − *Department of Materials Science, Fudan University, Shanghai 200433, P. R. China;* orcid.org/0000-0003-3387-4532; Email: xshfang@fudan.edu.cn

Authors

Yong Zhang − *Department of Materials Science, Fudan University, Shanghai 200433, P. R. China*

Siyuan Li − *Department of Materials Science, Fudan University, Shanghai 200433, P. R. China*

Ziliang Li − *Department of Materials Science, Fudan University, Shanghai 200433, P. R. China*

Hui Liu − *Department of Materials Science, Fudan University, Shanghai 200433, P. R. China*

Xinya Liu − *Department of Materials Science, Fudan University, Shanghai 200433, P. R. China*

Jiaxin Chen − *Department of Materials Science, Fudan University, Shanghai 200433, P. R. China*

Complete contact information is available at: https://pubs.acs.org/10.1021/acs.nanolett.0c03759

Author Contributions

The manuscript was written through contributions of all authors. All authors have given approval to the final version of the manuscript.

Notes

The authors declare no competing financial interest.

ACKNOWLEDGMENTS

This work was supported by National Key R&D Program of China (Nos. 2018YFA0703700 and 2017YFA0204600), Science and Technology Commission of Shanghai Municipality (Grant Nos. 18520744600, 19520744300 and 18520710800), the National Natural Science Foundation of China (51872050), and Ministry of Education Joint Fund for Equipment Pre-Research (No. 6141A02033241). Part of the experimental work was carried out in the Fudan Nanofabrication Laboratory.

REFERENCES

(1) Guo, F.; Yang, W.; Yuan, Y.; Xiao, Z.; Dong, Q.; Bi, Y.; Huang, J. A nanocomposite ultraviolet photodetector based on interfacial trap-controlled charge injection. *Nat. Nanotechnol.* **2012**, *7* (12), 798−802.

(2) Liu, X.; Gu, L.; Zhang, Q.; Wu, J.; Long, Y.; Fan, Z. All-printable band-edge modulated ZnO nanowire photodetectors with ultra-high detectivity. *Nat. Commun.* **2014**, *5*, 4007.

(3) Garcia de Arquer, F. P.; Armin, A.; Meredith, P.; Sargent, E. H. Solution-processed semiconductors for next-generation photodetectors. *Nat. Rev. Mater.* **2017**, *2* (3), 16100.

(4) Yang, W.; Hu, K.; Teng, F.; Weng, H.; Zhang, Y.; Fang, X. S. High-performance silicon-compatible large-area UV-to-visible broadband photodetector based on integrated lattice-matched type II Se/n-Si heterojunctions. *Nano Lett.* **2018**, *18* (8), 4697−4703.

(5) Cai, S.; Xu, X.; Yang, W.; Chen, J.; Fang, X. S. Materials and designs for wearable photodetectors. *Adv. Mater.* **2019**, *31* (18), 1808138.
(6) Nasiri, N.; Bo, R.; Wang, F.; Fu, L.; Tricoli, A. Ultraporous electron-depleted ZnO nanoparticle networks for highly sensitive portable visible-blind UV photodetectors. *Adv. Mater.* **2015**, *27* (29), 4336−4343.
(7) Kong, X.; Liu, C.; Dong, W.; Zhang, X.; Tao, C.; Shen, L.; Zhou, J.; Fei, Y.; Ruan, S. Metal-semiconductor-metal TiO_2 ultraviolet detectors with Ni electrodes. *Appl. Phys. Lett.* **2009**, *94* (12), 123502.
(8) Liu, K.; Sakurai, M.; Aono, M.; Shen, D. Ultrahigh-gain single SnO_2 microrod photoconductor on flexible substrate with fast recovery speed. *Adv. Funct. Mater.* **2015**, *25* (21), 3157−3163.
(9) Pearton, S.; Yang, J.; Cary IV, P.; Ren, F.; Kim, J.; Tadjer, M.; Mastro, M. A review of Ga_2O_3 materials, processing, and devices. *Appl. Phys. Rev.* **2018**, *5* (1), 011301.
(10) Li, L.; Zhang, Y.; Fang, X. S.; Zhai, T.; Liao, M.; Sun, X.; Koide, Y.; Bando, Y.; Golberg, D. WO_3 nanowires on carbon papers: electronic transport, improved ultraviolet-light photodetectors and excellent field emitters. *J. Mater. Chem.* **2011**, *21* (18), 6525−6530.
(11) Jin, Z.; Zhou, Q.; Chen, Y.; Mao, P.; Li, H.; Liu, H.; Wang, J.; Li, Y. Graphdiyne:ZnO nanocomposites for high-Performance UV photodetectors. *Adv. Mater.* **2016**, *28* (19), 3697−3702.
(12) Xie, C.; Lu, X.; Tong, X.; Zhang, Z.; Liang, F.; Liang, L.; Luo, L.; Wu, Y. Recent progress in solar-blind deep-ultraviolet photodetectors based on inorganic ultrawide bandgap semiconductors. *Adv. Funct. Mater.* **2019**, *29* (9), 1806006.
(13) Deka Boruah, B. Zinc oxide ultraviolet photodetectors: rapid progress from conventional to self-powered photodetectors. *Nanoscale Adv.* **2019**, *1* (6), 2059−2085.
(14) Nasiri, N.; Jin, D.; Tricoli, A. Nanoarchitechtonics of visible-blind ultraviolet photodetector materials: critical features and nano-microfabrication. *Adv. Opt. Mater.* **2019**, *7* (2), 1800580.
(15) Zhang, Y.; Xu, X.; Fang, X. S. Tunable self-powered n-$SrTiO_3$ photodetectors based on varying CuS-ZnS nanocomposite film (p-CuZnS, p-CuS, and n-ZnS). *InfoMat* **2019**, *1* (4), 542.
(16) Zhang, Y.; Zhao, X.; Chen, J.; Li, S.; Yang, W.; Fang, X. S. Self-polarized $BaTiO_3$ for greatly enhanced performance of ZnO UV photodetector by regulating the distribution of electron concentration. *Adv. Funct. Mater.* **2020**, *30* (5), 1907650.
(17) Lin, Z.; Liu, Y.; Halim, U.; Ding, M.; Liu, Y.; Wang, Y.; Jia, C.; Chen, P.; Duan, X.; Wang, C.; Song, F.; Li, M.; Wan, C.; Huang, Y.; Duan, X. Solution-processable 2D semiconductors for high-performance large-area electronics. *Nature* **2018**, *562* (7726), 254−258.
(18) Bae, S.; Kum, H.; Kong, W.; Kim, Y.; Choi, C.; Lee, B.; Lin, P.; Park, Y.; Kim, J. Integration of bulk materials with two-dimensional materials for physical coupling and applications. *Nat. Mater.* **2019**, *18* (6), 550−560.
(19) Zhou, X.; Hu, X.; Zhou, S.; Song, H.; Zhang, Q.; Pi, L.; Li, L.; Li, H.; Lü, J.; Zhai, T. Tunneling diode based on WSe_2/SnS_2 heterostructure incorporating high detectivity and responsivity. *Adv. Mater.* **2018**, *30* (7), 1703286.
(20) Velusamy, D. B.; Haque, M. A.; Parida, M. R.; Zhang, F.; Wu, T.; Mohammed, O. F.; Alshareef, H. N. 2D Organic-Inorganic Hybrid Thin Films for Flexible UV-Visible Photodetectors. *Adv. Funct. Mater.* **2017**, *27* (15), 1605554.
(21) Maculan, G.; Sheikh, A. D.; Abdelhady, A. L.; Saidaminov, M. I.; Haque, M. A.; Murali, B.; Alarousu, E.; Mohammed, O. F.; Wu, T.; Bakr, O. M. $CH_3NH_3PbCl_3$ single crystals: inverse temperature crystallization and visible-blind UV-photodetector. *J. Phys. Chem. Lett.* **2015**, *6* (19), 3781−3786.
(22) Fu, Y.; Zhu, H.; Chen, J.; Hautzinger, M.; Zhu, X.; Jin, S. Metal halide perovskite nanostructures for optoelectronic applications and the study of physical properties. *Nat. Rev. Mater.* **2019**, *4* (3), 169−188.
(23) Cheng, B.; Li, T.; Wei, P.; Yin, J.; Ho, K.; Retamal, J.; Mohammed, Q.; He, J. Layer-edge device of two-dimensional hybrid perovskites. *Nat. Commun.* **2018**, *9*, 5196.
(24) Do, T. T. H.; Granados del Aguila, A. G.; Zhang, D.; Xing, H.; Liu, S.; Prosnikov, M. A.; Gao, W. B.; Chang, K.; Christianen, P. C. M.; Xiong, Q. H. Bright exciton fine-structure in two-dimensional lead halide perovskites. *Nano Lett.* **2020**, *20* (7), 5141−5148.
(25) Li, B.; Osada, M.; Ebina, Y.; Ueda, S.; Sasaki, T. Coexistence of magnetic order and ferroelectricity at 2D nanosheet interfaces. *J. Am. Chem. Soc.* **2016**, *138* (24), 7621−7625.
(26) Kim, Y.; Kim, H.; Osada, M.; Li, B.; Ebina, Y.; Sasaki, T. 2D perovskite nanosheets with thermally-stable high-κ response: A new platform for high-temperature capacitors. *ACS Appl. Mater. Interfaces* **2014**, *6* (22), 19510−19514.
(27) Oshima, T.; Lu, D.; Maeda, K. Preparation of Pt-intercalated $KCa_2Nb_3O_{10}$ nanosheets and their photocatalytic activity for overall water splitting. *ChemNanoMat* **2016**, *2* (7), 748−755.
(28) Li, B.; Osada, M.; Ebina, Y.; Akatsuka, K.; Fukuda, K.; Sasaki, T. High thermal robustness of molecularly thin perovskite nanosheets and implications for superior dielectric properties. *ACS Nano* **2014**, *8* (6), 5449−5461.
(29) Maeda, K.; Sahara, G.; Eguchi, M.; Ishitani, O. Hybrids of a ruthenium(II) polypyridyl complex and a metal oxide nanosheet for dye-sensitized hydrogen evolution with visible light: effects of the energy structure on photocatalytic activity. *ACS Catal.* **2015**, *5* (3), 1700−1707.
(30) Maeda, K.; Eguchi, M.; Oshima, T. Perovskite oxide nanosheets with tunable band-edge potentials and high photocatalytic hydrogen-evolution activity. *Angew. Chem., Int. Ed.* **2014**, *53* (48), 13164−13168.
(31) Liu, H.; Gao, N.; Liao, M.; Fang, X. S. Hexagonal-like Nb_2O_5 nanoplates-based photodetectors and photocatalyst with high performances. *Sci. Rep.* **2015**, *5*, 7716.
(32) Liu, H.; Zhang, Z.; Hu, L.; Gao, N.; Sang, L.; Liao, M.; Ma, R.; Xu, F.; Fang, X. S. New UV-A photodetector based on individual potassium niobate nanowires with high performance. *Adv. Opt. Mater.* **2014**, *2* (8), 771−778.
(33) Compton, O.; Osterloh, F. Niobate nanosheets as catalysts for photochemical water splitting into hydrogen and hydrogen peroxide. *J. Phys. Chem. C* **2009**, *113* (1), 479−485.
(34) Gedamu, D.; Paulowicz, I.; Kaps, S.; Lupan, O.; Wille, S.; Haidarschin, G.; Mishra, Y.; Adelung, R. Rapid fabrication technique for interpenetrated ZnO nanotetrapod networks for fast UV sensors. *Adv. Mater.* **2014**, *26* (10), 1541−1550.
(35) Xu, P.; Milstein, T.; Mallouk, T. Flat-band potentials of molecularly thin metal oxide nanosheets. *ACS Appl. Mater. Interfaces* **2016**, *8* (18), 11539−11548.
(36) Zhao, B.; Wang, F.; Chen, H.; Zheng, L.; Su, L.; Zhao, D.; Fang, X. S. An ultrahigh responsivity (9.7 mA W^{-1}) self-powered solar-blind photodetector based on individual ZnO-Ga_2O_3 heterostructures. *Adv. Funct. Mater.* **2017**, *27* (17), 1700264.
(37) Li, Z.; Qiao, H.; Guo, Z.; Ren, X.; Huang, Z.; Qi, X.; Dhanabalan, S.; Ponraj, J.; Zhang, D.; Li, J.; Zhao, J.; Zhong, J.; Zhang, H. High-performance photo-electrochemical photodetector based on liquid-exfoliated few-layered InSe nanosheets with enhanced stability. *Adv. Funct. Mater.* **2018**, *28* (16), 1705237.
(38) Ren, X.; Li, Z.; Huang, Z.; Sang, D.; Qiao, H.; Qi, X.; Li, J.; Zhong, J.; Zhang, H. Environmentally robust black phosphorus nanosheets in solution: application for self-powered photodetector. *Adv. Funct. Mater.* **2017**, *27* (18), 1606834.
(39) Howard, I.; Abzieher, T.; Hossain, I.; Eggers, H.; Schackmar, F.; Ternes, S.; Richards, B.; Lemmer, U.; Paetzold, U. Coated and printed perovskites for photovoltaic applications. *Adv. Mater.* **2019**, *31* (26), 1806702.
(40) Park, B.; Seok, S. Intrinsic instability of inorganic−organic hybrid halide perovskite materials. *Adv. Mater.* **2019**, *31* (20), 1805337.

https://dx.doi.org/10.1021/acs.nanolett.0c03759
Nano Lett. 2021, 21, 382−388